
Improving robustness to corruptions with multiplicative weight perturbations

Trung Trinh¹ Markus Heinonen¹ Luigi Acerbi² Samuel Kaski^{1,3}

¹Department of Computer Science, Aalto University, Finland

²Department of Computer Science, University of Helsinki, Finland

³Department of Computer Science, University of Manchester, United Kingdom

{trung.trinh, markus.o.heinonen, samuel.kaski}@aalto.fi,
luigi.acerbi@helsinki.fi

Abstract

Deep neural networks (DNNs) excel on clean images but struggle with corrupted ones. Incorporating specific corruptions into the data augmentation pipeline can improve robustness to those corruptions but may harm performance on clean images and other types of distortion. In this paper, we introduce an alternative approach that improves the robustness of DNNs to a wide range of corruptions without compromising accuracy on clean images. We first demonstrate that input perturbations can be mimicked by multiplicative perturbations in the weight space. Leveraging this, we propose Data Augmentation via Multiplicative Perturbation (DAMP), a training method that optimizes DNNs under random multiplicative weight perturbations. We also examine the recently proposed Adaptive Sharpness-Aware Minimization (ASAM) and show that it optimizes DNNs under adversarial multiplicative weight perturbations. Experiments on image classification datasets (CIFAR-10/100, TinyImageNet and ImageNet) and neural network architectures (ResNet50, ViT-S/16) show that DAMP enhances model generalization performance in the presence of corruptions across different settings. Notably, DAMP is able to train a ViT-S/16 on ImageNet from scratch, reaching the top-1 error of 23.7% which is comparable to ResNet50 without extensive data augmentations.

1 Introduction

Deep neural networks (DNNs) demonstrate impressive accuracy in computer vision tasks when evaluated on carefully curated and clean datasets. However, their performance significantly declines when test images are affected by natural distortions such as camera noise, changes in lighting and weather conditions, or image compression algorithms (Hendrycks and Dietterich, 2019). This drop in performance is problematic in production settings, where models inevitably encounter such perturbed inputs. Therefore, it is crucial to develop methods that produce reliable DNNs robust to common image corruptions, particularly for deployment in safety-critical systems (Amodei et al., 2016).

To enhance robustness against a specific corruption, one could simply include it in the data augmentation pipeline during training. However, this approach can diminish performance on clean images and reduce robustness to other types of corruptions (Geirhos et al., 2018). More advanced data augmentation techniques (Cubuk et al., 2018; Hendrycks et al., 2019; Lopes et al., 2019) have been developed which effectively enhance corruption robustness without compromising accuracy on clean images. Nonetheless, a recent study by Mintun et al. (2021) has identified a new set of image corruptions to which models trained with these techniques remain vulnerable. Besides data augmentation, ensemble methods such as Deep ensembles and Bayesian neural networks have also been shown to improve generalization in the presence of corruptions (Lakshminarayanan et al., 2017;

Ovadia et al., 2019; Dusenberry et al., 2020; Trinh et al., 2022). However, the training and inference costs of these methods increase linearly with the number of ensemble members, rendering them less suitable for very large DNNs.

Contributions In this work, we show that simply perturbing weights with random multiplicative noises during training can significantly improve robustness to a wide range of corruptions. Our contributions are as follows:

- We show in Section 2 that the effects of input corruptions can be simulated during training via multiplicative weight perturbations.
- From this insight, we propose a new training algorithm called Data Augmentation via Multiplicative Perturbations (DAMP) which perturbs weights using random multiplicative Gaussian noise during training while having the same training cost as standard SGD.
- In Section 3, we show a connection between adversarial multiplicative weight perturbations and Adaptive Sharpness-Aware Minimization (ASAM) (Kwon et al., 2021).
- Through a rigorous empirical study in Section 4, we demonstrate that DAMP consistently improves generalization ability of DNNs under corruptions across different image classification datasets and model architectures.
- Notably, we demonstrate that DAMP can train a Vision Transformer (ViT) (Dosovitskiy et al., 2021) from scratch on ImageNet, achieving similar accuracy to a ResNet50 (He et al., 2016a) in 200 epochs with only basic Inception-style preprocessing (Szegedy et al., 2016). This is significant as ViT typically requires advanced training methods or sophisticated data augmentation to match ResNet50’s performance when being trained on ImageNet from scratch (Chen et al., 2022; Beyer et al., 2022).

2 Data Augmentation via Multiplicative Perturbations

In this section, we show that one can simulate the effect of input corruptions during training via multiplicative weight perturbations. Given a training data set $\mathcal{S} = \{(\mathbf{x}_k, y_k)\}_{k=1}^N \subseteq \mathcal{X} \times \mathcal{Y}$ drawn i.i.d. from the data distribution \mathcal{D} , we seek to learn a model that generalizes well on both clean and corrupted inputs. We denote \mathcal{G} as a set of functions whose each member $\mathbf{g} : \mathcal{X} \rightarrow \mathcal{X}$ represents an input corruption. That is, for each $\mathbf{x} \in \mathcal{X}$, $\mathbf{g}(\mathbf{x})$ is a corrupted version of \mathbf{x} .¹ We define $\mathbf{g}(\mathcal{S}) \stackrel{\text{def}}{=} \{(\mathbf{g}(\mathbf{x}_k), y_k)\}_{k=1}^N$ as the training set corrupted by \mathbf{g} . We consider a fully-connected neural network $\mathbf{f}(\mathbf{x}; \boldsymbol{\omega})$ of depth H parameterized by $\boldsymbol{\omega} = \{\mathbf{W}^{(h)}\}_{h=1}^H \in \mathcal{W}$, which we define recursively as follows:

$$\mathbf{f}^{(0)}(\mathbf{x}) \stackrel{\text{def}}{=} \mathbf{x}, \tag{1}$$

$$\mathbf{z}^{(h)}(\mathbf{x}) \stackrel{\text{def}}{=} \mathbf{W}^{(h)} \mathbf{f}^{(h-1)}(\mathbf{x}), \quad \mathbf{f}^{(h)}(\mathbf{x}) \stackrel{\text{def}}{=} \boldsymbol{\sigma}^{(h)}(\mathbf{z}^{(h)}(\mathbf{x})), \quad \forall h = 1, \dots, H \tag{2}$$

$$\mathbf{f}(\mathbf{x}; \boldsymbol{\omega}) \stackrel{\text{def}}{=} \mathbf{f}^{(H)}(\mathbf{x}). \tag{3}$$

where $\boldsymbol{\sigma}^{(h)}$ is the non-linear activation of layer h . Given a per-sample loss $\ell : \mathcal{W} \times \mathcal{X} \times \mathcal{Y} \rightarrow \mathbb{R}_+$, the training loss is defined as the average loss over the samples $\mathcal{L}(\boldsymbol{\omega}; \mathcal{S}) \stackrel{\text{def}}{=} \frac{1}{N} \sum_{k=1}^N \ell(\boldsymbol{\omega}, \mathbf{x}_k, y_k)$. Our goal is to find $\boldsymbol{\omega}$ which minimizes:

$$\mathcal{L}(\boldsymbol{\omega}; \mathcal{G}(\mathcal{S})) \stackrel{\text{def}}{=} \mathbb{E}_{\mathbf{g} \sim \mathcal{G}} [\mathcal{L}(\boldsymbol{\omega}; \mathbf{g}(\mathcal{S}))] \tag{4}$$

Now we show that the effect of each corruption \mathbf{g} can be simulated during training with multiplicative weight perturbations. To this end, we study how input corruption affects the training loss. We use the following two assumptions for our analysis:

Assumption 1. For each corruption function $\mathbf{g} : \mathcal{X} \rightarrow \mathcal{X}$ in \mathcal{G} , there exists a constant $M > 0$ such that $\|\mathbf{g}(\mathbf{x}) - \mathbf{x}\|_2 \leq M$ for all $\mathbf{x} \in \mathcal{X}$.

Assumption 2. The gradient of the per-sample loss with respect to the input $\nabla_{\mathbf{x}} \ell(\boldsymbol{\omega}, \mathbf{x}, y)$ is Lipschitz continuous.

¹For instance, if \mathbf{x} is a clean image then $\mathbf{g}(\mathbf{x})$ could be \mathbf{x} corrupted by *Gaussian noise*.

Assumption 1 means that the corruption \mathbf{g} does not substantially alter the input \mathbf{x} , which is true for images since the values of image pixels are bounded between 0 and 1. Assumption 2 allows us to define a quadratic bound of the loss function using a second-order Taylor expansion. We first notice that the corruption \mathbf{g} causes a shift $\delta_{\mathbf{g}}\mathbf{f}^{(0)}(\mathbf{x}) \stackrel{\text{def}}{=} \mathbf{g}(\mathbf{x}) - \mathbf{x}$ in the input \mathbf{x} which leads to shifts in the output of each layer during the forward pass:

$$\underbrace{\delta_{\mathbf{g}}\mathbf{f}^{(h)}(\mathbf{x})}_{\text{shift}} \stackrel{\text{def}}{=} \underbrace{\mathbf{f}^{(h)}(\mathbf{g}(\mathbf{x}))}_{\text{corrupted output}} - \underbrace{\mathbf{f}^{(h)}(\mathbf{x})}_{\text{clean output}} \quad (5)$$

This will eventually cause a shift in the per-sample loss $\delta_{\mathbf{g}}\ell(\boldsymbol{\omega}, \mathbf{x}, y) \stackrel{\text{def}}{=} \ell(\boldsymbol{\omega}, \mathbf{g}(\mathbf{x}), y) - \ell(\boldsymbol{\omega}, \mathbf{x}, y)$. Using Assumptions 1 and 2, we prove the following lemma which characterizes the connection between $\delta_{\mathbf{g}}\ell(\boldsymbol{\omega}, \mathbf{x}, y)$ and $\delta_{\mathbf{g}}\mathbf{f}^{(h)}(\mathbf{x})$:

Lemma 1. *For all $h = 1, \dots, H$ and for all $\mathbf{x} \in \mathcal{X}$, there exists a scalar $C_{\mathbf{g}}^{(h)}(\mathbf{x}) > 0$ such that:*

$$\delta_{\mathbf{g}}\ell(\boldsymbol{\omega}, \mathbf{x}, y) \leq \left\langle \nabla_{\mathbf{z}^{(h+1)}}\ell(\boldsymbol{\omega}, \mathbf{x}, y) \otimes \delta_{\mathbf{g}}\mathbf{f}^{(h)}(\mathbf{x}), \mathbf{W}^{(h+1)} \right\rangle_F + \frac{C_{\mathbf{g}}^{(h)}(\mathbf{x})}{2} \|\mathbf{W}^{(h)}\|_F^2 \quad (6)$$

Here \otimes denotes the outer product of two vectors, $\langle \cdot, \cdot \rangle_F$ denotes the Frobenius inner product of two matrices of the same dimension, $\|\cdot\|_F$ is the Frobenius norm, and $\nabla_{\mathbf{z}^{(h)}}\ell(\boldsymbol{\omega}, \mathbf{x}, y)$ is the Jacobian of the per-sample loss with respect to the pre-activation output $\mathbf{z}^{(h)}(\mathbf{x})$ at layer h . The proof of Lemma 1 is provided in Appendix A. Using Lemma 1, we prove the following theorem, which bounds the training loss in the presence of corruptions using the training loss under multiplicative perturbations in the weight space:

Theorem 1. *For a function $\mathbf{g} : \mathcal{X} \rightarrow \mathcal{X}$ satisfying Assumption 1 and a loss function \mathcal{L} satisfying Assumption 2, there exists $\boldsymbol{\xi}_g \in \mathcal{W}$ and $C_g > 0$ such that:*

$$\mathcal{L}(\boldsymbol{\omega}; \mathbf{g}(\mathcal{S})) \leq \mathcal{L}(\boldsymbol{\omega} \circ \boldsymbol{\xi}_g; \mathcal{S}) + \frac{C_g}{2} \|\boldsymbol{\omega}\|_F^2 \quad (7)$$

where \circ denotes the Hadamard product.

Proof. From Lemma 1, we have for all $h = 0, \dots, H-1$:

$$\mathcal{L}(\boldsymbol{\omega}; \mathbf{g}(\mathcal{S})) = \frac{1}{N} \sum_{k=1}^N \ell(\boldsymbol{\omega}, \mathbf{g}(\mathbf{x}_k), y_k) = \frac{1}{N} \sum_{k=1}^N \left(\ell(\boldsymbol{\omega}, \mathbf{x}_k, y_k) + \delta_{\mathbf{g}}\ell(\boldsymbol{\omega}, \mathbf{x}_k, y_k) \right) \quad (8)$$

$$\leq \mathcal{L}(\boldsymbol{\omega}; \mathcal{S}) + \frac{1}{N} \sum_{k=1}^N \left\langle \nabla_{\mathbf{z}^{(h+1)}}\ell(\boldsymbol{\omega}, \mathbf{x}_k, y_k) \otimes \delta_{\mathbf{g}}\mathbf{f}^{(h)}(\mathbf{x}_k), \mathbf{W}^{(h+1)} \right\rangle_F + \frac{\hat{C}_{\mathbf{g}}^{(h)}}{2} \|\mathbf{W}^{(h)}\|_F^2 \quad (9)$$

where $\hat{C}_{\mathbf{g}}^{(h)} = \max_{\mathbf{x} \in \mathcal{S}} C_{\mathbf{g}}^{(h)}(\mathbf{x})$. Since this bound is true for all h , we can take the average:

$$\begin{aligned} \mathcal{L}(\boldsymbol{\omega}; \mathbf{g}(\mathcal{S})) &\leq \mathcal{L}(\boldsymbol{\omega}; \mathcal{S}) + \frac{1}{H} \sum_{h=1}^H \frac{1}{N} \sum_{k=1}^N \left\langle \nabla_{\mathbf{z}^{(h)}}\ell(\boldsymbol{\omega}, \mathbf{x}_k, y_k) \otimes \delta_{\mathbf{g}}\mathbf{f}^{(h-1)}(\mathbf{x}_k), \mathbf{W}^{(h)} \right\rangle_F \\ &\quad + \frac{C_{\mathbf{g}}}{2} \|\boldsymbol{\omega}\|_F^2 \quad (10) \end{aligned}$$

where $C_g = \frac{1}{H} \sum_{h=1}^H \hat{C}_{\mathbf{g}}^{(h)}$. The right-hand side of Eq. (10) can be written as:

$$\mathcal{L}(\boldsymbol{\omega}; \mathcal{S}) + \frac{1}{H} \sum_{h=1}^H \left\langle \frac{1}{N} \sum_{k=1}^N \nabla_{\mathbf{z}^{(h)}}\ell(\boldsymbol{\omega}, \mathbf{x}_k, y_k) \otimes \delta_{\mathbf{g}}\mathbf{f}^{(h-1)}(\mathbf{x}_k), \mathbf{W}^{(h)} \right\rangle_F + \frac{C_g}{2} \|\boldsymbol{\omega}\|_F^2 \quad (11)$$

$$= \mathcal{L}(\boldsymbol{\omega}; \mathcal{S}) + \sum_{h=1}^H \left\langle \nabla_{\mathbf{W}^{(h)}}\mathcal{L}(\boldsymbol{\omega}; \mathcal{S}), \mathbf{W}^{(h)} \circ \boldsymbol{\xi}^{(h)}(\mathbf{g}) \right\rangle_F + \frac{C_g}{2} \|\boldsymbol{\omega}\|_F^2 \quad (12)$$

$$\leq \mathcal{L}(\boldsymbol{\omega} + \boldsymbol{\omega} \circ \boldsymbol{\xi}(\mathbf{g}); \mathcal{S}) + \frac{C_g}{2} \|\boldsymbol{\omega}\|_F^2 = \mathcal{L}(\boldsymbol{\omega} \circ (1 + \boldsymbol{\xi}(\mathbf{g})); \mathcal{S}) + \frac{C_g}{2} \|\boldsymbol{\omega}\|_F^2 \quad (13)$$

Algorithm 1 DAMP: Data Augmentation via Multiplicative Perturbations

- 1: **Input:** training data $\mathcal{S} = \{\mathbf{x}_k, y_k\}_{k=1}^N$, a neural network $\mathbf{f}(\cdot; \boldsymbol{\omega})$ parameterized by $\boldsymbol{\omega} \in \mathbb{R}^P$, number of iterations T , step sizes $\{\eta_t\}_{t=1}^T$, number of sub-batch M , batch size B divisible by M , a noise distribution $\Xi = \mathcal{N}(\mathbf{1}, \sigma^2 \mathbf{I}_P)$, weight decay coefficient λ , a loss function $\mathcal{L} : \mathbb{R}^P \rightarrow \mathbb{R}_+$.
 - 2: **Output:** Optimized parameter $\boldsymbol{\omega}^{(T)}$.
 - 3: Initialize parameter $\boldsymbol{\omega}^{(0)}$.
 - 4: **for** $t = 1$ **to** T **do**
 - 5: Draw a mini-batch $\mathcal{B} = \{\mathbf{x}_b, y_b\}_{b=1}^B \sim \mathcal{S}$.
 - 6: Divide the mini-batch into M disjoint sub-batches $\{\mathcal{B}_m\}_{m=1}^M$ of equal size.
 - 7: **for** $m = 1$ **to** M **in parallel do**
 - 8: Draw a noise sample $\boldsymbol{\xi}_m \sim \Xi$.
 - 9: Compute the gradient $\mathbf{g}_m = \nabla_{\boldsymbol{\omega}} \mathcal{L}(\boldsymbol{\omega}; \mathcal{B}_m) \Big|_{\boldsymbol{\omega}^{(t)} \circ \boldsymbol{\xi}_m}$.
 - 10: **end for**
 - 11: Compute the average gradient: $\mathbf{g} = \frac{1}{M} \sum_{m=1}^M \mathbf{g}_m$.
 - 12: Update the weights: $\boldsymbol{\omega}^{(t+1)} = \boldsymbol{\omega}^{(t)} - \eta_t (\mathbf{g} + \lambda \boldsymbol{\omega}^{(t)})$.
 - 13: **end for**
-

where $\boldsymbol{\xi}^{(h)}(\mathbf{g})$ is a matrix of the same dimension as $\mathbf{W}^{(h)}$ whose each entry is defined as:

$$\left[\boldsymbol{\xi}^{(h)}(\mathbf{g}) \right]_{i,j} = \frac{1}{H} \frac{\left[\sum_{k=1}^N \nabla_{\mathbf{z}^{(h)}} \ell(\boldsymbol{\omega}, \mathbf{x}_k, y_k) \otimes \boldsymbol{\delta}_{\mathbf{g}} \mathbf{f}^{(h-1)}(\mathbf{x}_k) \right]_{i,j}}{\left[\sum_{k=1}^N \nabla_{\mathbf{z}^{(h)}} \ell(\boldsymbol{\omega}, \mathbf{x}_k, y_k) \otimes \mathbf{f}^{(h-1)}(\mathbf{x}_k) \right]_{i,j}} \quad (14)$$

The inequality in Eq. (13) is due to the first-order Taylor expansion and the assumption that the training loss is locally convex at $\boldsymbol{\omega}$. This assumption is expected to hold for the final solution but does not necessarily hold for any $\boldsymbol{\omega}$. Eq. (7) is obtained by combining Eq. (10) and Eq. (13). \square

Theorem 1 provides an upper bound to the target loss in Eq. (4):

$$\mathcal{L}(\boldsymbol{\omega}; \mathcal{G}(\mathcal{S})) \leq \mathbb{E}_{\mathbf{g} \sim \mathcal{G}} \left[\mathcal{L}(\boldsymbol{\omega} \circ (1 + \boldsymbol{\xi}(\mathbf{g})); \mathcal{S}) + \frac{C_{\mathbf{g}}}{2} \|\boldsymbol{\omega}\|_F^2 \right] \quad (15)$$

This bound suggests that in a scenario where we do not have any information regarding the set of corruptions \mathcal{G} , we can simulate \mathcal{G} using random multiplicative weight perturbations, leading to the following proxy loss:

$$\mathcal{L}_{\Xi}(\boldsymbol{\omega}; \mathcal{S}) \stackrel{\text{def}}{=} \mathbb{E}_{\boldsymbol{\xi} \sim \Xi} [\mathcal{L}(\boldsymbol{\omega} \circ \boldsymbol{\xi}; \mathcal{S})] + \frac{\lambda}{2} \|\boldsymbol{\omega}\|_F^2 \quad (16)$$

We note that the second term in Eq. (16) is the L_2 -regularization commonly used in optimizing DNNs. Based on this proxy loss, we propose Algorithm 1 which minimizes the objective function in Eq. (16) when Ξ is an isotropic Gaussian distribution $\mathcal{N}(\mathbf{1}, \sigma^2 \mathbf{I})$. We call this algorithm Data Augmentation via Multiplicative Perturbations (DAMP), as it uses random multiplicative weight perturbations during training to simulate input corruptions, which can be viewed as data augmentations.

Remark The standard method to calculate the expected loss in Eq. (16), which lacks a closed-form solution, is the Monte Carlo (MC) approximation. However, the training cost of this approach scales linearly with the number of MC samples. To match the training cost of standard SGD, Algorithm 1 divides each data batch into M equal sub-batches (Line 6) and calculates the loss on each sub-batch with different multiplicative noises from the noise distribution Ξ (Lines 7–9). The final gradient is obtained by averaging the sub-batch gradients (Line 11). Algorithm 1 is thus suitable for data parallelism in multi-GPU training, where the data batch is evenly distributed across $M > 1$ GPUs. Compared to SGD, Algorithm 1 requires only two additional operations: generating Gaussian samples and point-wise multiplication, both of which have negligible computational costs. In our experiments, we found that both SGD and DAMP had similar training times.

3 Adaptive Sharpness-Aware Minimization optimizes DNNs under adversarial multiplicative weight perturbations

In this section, we demonstrate that optimizing DNNs with adversarial multiplicative weight perturbations follows a similar update rule to Adaptive Sharpness-Aware Minimization (ASAM) (Kwon et al., 2021). We first provide a brief description of ASAM and its predecessor Sharpness-Aware Minimization (SAM) (Foret et al., 2021):

SAM Motivated by previous findings that wide optima tend to generalize better than sharp ones (Keskar et al., 2017; Jiang et al., 2020), SAM regularizes the sharpness of an optimum by solving the following minimax optimization:

$$\min_{\omega} \max_{\|\xi\|_2 \leq \rho} \mathcal{L}(\omega + \xi; \mathcal{S}) + \frac{\lambda}{2} \|\omega\|_F^2 \quad (17)$$

which can be interpreted as optimizing DNNs under adversarial additive perturbations. To efficiently solve this problem, Foret et al. (2021) devise a two-step procedure for each iteration t :

$$\xi^{(t)} = \rho \frac{\nabla_{\omega} \mathcal{L}(\omega^{(t)}; \mathcal{S})}{\|\nabla_{\omega} \mathcal{L}(\omega^{(t)}; \mathcal{S})\|_2}, \quad \omega^{(t+1)} = \omega^{(t)} - \eta_t \left(\nabla_{\omega} \mathcal{L}(\omega^{(t)} + \xi^{(t)}; \mathcal{S}) + \lambda \omega^{(t)} \right) \quad (18)$$

where η_t is the learning rate. Each iteration of SAM thus takes twice as long to run than SGD.

ASAM Kwon et al. (2021) note that SAM attempts to minimize the maximum loss over a rigid sphere of radius ρ around an optimum, which is not suitable for ReLU networks since their parameters can be freely re-scaled without affecting the outputs. The authors thus propose ASAM as an alternative optimization problem to SAM which regularizes the *adaptive sharpness* of an optimum:

$$\min_{\omega} \max_{\|T_{\omega}^{-1} \xi\|_2 \leq \rho} \mathcal{L}(\omega + \xi; \mathcal{S}) + \frac{\lambda}{2} \|\omega\|_F^2 \quad (19)$$

where T_{ω} is an invertible linear operator used to reshape the perturbation region (so that it is not necessarily a sphere as in SAM). Kwon et al. (2021) found that $T_{\omega} = |\omega|$ produced the best results. Solving Eq. (19) in this case leads to the following two-step procedure for each iteration t :

$$\hat{\xi}^{(t)} = \rho \frac{(\omega^{(t)})^2 \circ \nabla_{\omega} \mathcal{L}(\omega^{(t)}; \mathcal{S})}{\|\omega^{(t)} \circ \nabla_{\omega} \mathcal{L}(\omega^{(t)}; \mathcal{S})\|_2}, \quad \omega^{(t+1)} = \omega^{(t)} - \eta_t \left(\nabla_{\omega} \mathcal{L}(\omega^{(t)} + \hat{\xi}^{(t)}; \mathcal{S}) + \lambda \omega^{(t)} \right) \quad (20)$$

Similar to SAM, each iteration of ASAM also takes twice as long to run than SGD.

ASAM and adversarial multiplicative perturbations Algorithm 1 minimizes the expected loss in Eq. (16). Instead, we could minimize the loss under the adversarial multiplicative weight perturbation:

$$\mathcal{L}_{\max}(\omega; \mathcal{S}) \stackrel{\text{def}}{=} \max_{\|\xi\|_2 \leq \rho} \mathcal{L}(\omega + \omega \circ \xi; \mathcal{S}) \quad (21)$$

Similar to Foret et al. (2021), we solve this optimization problem by using a first-order Taylor expansion of $\mathcal{L}(\omega + \omega \circ \xi; \mathcal{S})$ to find an approximate solution of the inner maximization:

$$\arg \max_{\|\xi\|_2 \leq \rho} \mathcal{L}(\omega + \omega \circ \xi; \mathcal{S}) \approx \arg \max_{\|\xi\|_2 \leq \rho} \mathcal{L}(\omega; \mathcal{S}) + \langle \omega \circ \xi, \nabla_{\omega} \mathcal{L}(\omega; \mathcal{S}) \rangle \quad (22)$$

The maximizer of the Taylor expansion is:

$$\hat{\xi}(\omega) = \rho \frac{\omega \circ \nabla_{\omega} \mathcal{L}(\omega; \mathcal{S})}{\|\omega \circ \nabla_{\omega} \mathcal{L}(\omega; \mathcal{S})\|_2} \quad (23)$$

Substituting back into Eq. (21) and differentiating, we get:

$$\nabla_{\omega} \mathcal{L}_{\max}(\omega; \mathcal{S}) \approx \nabla_{\omega} \mathcal{L}(\omega + \omega \circ \hat{\xi}(\omega); \mathcal{S}) = \nabla_{\omega} \left(\omega + \omega \circ \hat{\xi}(\omega) \right) \nabla_{\omega} \mathcal{L}(\omega; \mathcal{S}) \Big|_{\omega + \omega \circ \hat{\xi}(\omega)} \quad (24)$$

$$= \nabla_{\hat{\omega}} \mathcal{L}(\hat{\omega}; \mathcal{S}) + \nabla_{\omega} \left(\omega \circ \hat{\xi}(\omega) \right) \nabla_{\omega} \mathcal{L}(\hat{\omega}; \mathcal{S}) \quad (25)$$

where $\hat{\omega}$ is the perturbed weight:

$$\hat{\omega} = \omega + \omega \circ \hat{\xi}(\omega) = \omega + \frac{\omega^2 \circ \nabla_{\omega} \mathcal{L}(\omega; \mathcal{S})}{\|\omega \circ \nabla_{\omega} \mathcal{L}(\omega; \mathcal{S})\|_2} \quad (26)$$

By omitting the second summand in Eq. (25), we arrive at the gradient formula in the update rule of ASAM in Eq. (20). We have thus established a connection between ASAM and adversarial multiplicative weight perturbations.

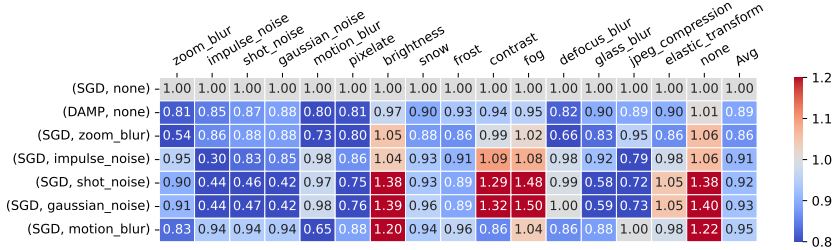


Figure 1: **DAMP improves robustness to all corruptions while preserving accuracy on clean images.** Results of ResNet18/CIFAR-100 experiments averaged over 5 seeds. The heatmap shows CE_c^f described in Eq. (27) (lower is better), where each row corresponds to a tuple of training (method, corruption), while each column corresponds to the test corruption. The Avg column shows the average of the results of the previous columns. none indicates no corruption. We use the models trained under the SGD/none setting (first row) as baselines to calculate the CE_c^f . The last five rows are the 5 best training corruptions ranked by the results in the Avg column.

4 Empirical evaluation

In this section, we assess the corruption robustness of DAMP and ASAM in image classification tasks. We conduct experiments using the CIFAR-10/100 (Krizhevsky, 2009), TinyImageNet (Le and Yang, 2015), and ImageNet (Deng et al., 2009) datasets. For evaluation on corrupted images, we utilize the CIFAR-10/100-C, TinyImageNet-C, and ImageNet-C datasets provided by Hendrycks and Dietterich (2019), as well as the ImageNet-C dataset provided by Mintun et al. (2021). The datasets from Hendrycks and Dietterich (2019) contain 15 common image corruptions, while ImageNet-C offers 10 additional corruptions. All corruptions in these datasets have 5 levels of severity. In terms of architectures, we use ResNet18 (He et al., 2016a) for CIFAR-10/100, PreActResNet18 (He et al., 2016b) for TinyImageNet, and ResNet50 (He et al., 2016a) and ViT-S/16 (Dosovitskiy et al., 2021) for ImageNet. We ran all experiments on a single machine with 8 Nvidia V100 GPUs. Detailed information for each experiment is provided in Appendix D.

4.1 Comparing DAMP to directly using corruptions as augmentations

In this section, we compare the corruption robustness of DNNs trained using DAMP with those trained directly on corrupted images. To train models on corrupted images, we utilize Algorithm 2 described in the Appendix. For a given target corruption g , Algorithm 2 randomly selects half the images in each training batch and applies g to them. This random selection process enhances the final model’s robustness to the target corruption while maintaining its accuracy on clean images. We use the `imagecorruptions` library (Michaelis et al., 2019) to apply the corruptions during training.

Evaluation metric We use the corruption error CE_c^f (Hendrycks and Dietterich, 2019) which measures the predictive error of classifier f in the presence of corruption c . Denote $E_{s,c}^f$ as the error of classifier f under corruption c with corruption severity s , the corruption error CE_c^f is defined as:

$$CE_c^f = \left(\sum_{s=1}^5 E_{s,c}^f \right) / \left(\sum_{s=1}^5 E_{s,c}^{f_{\text{baseline}}} \right) \quad (27)$$

For this metric, lower is better. Here f_{baseline} is a baseline classifier whose usage is to make the error more comparable between corruptions as some corruptions can be more challenging than others (Hendrycks and Dietterich, 2019). For each experiment setting, we use the model trained by SGD without corruptions as f_{baseline} .

Results We visualize the results for the ResNet18/CIFAR-100 setting in Fig. 1. The results for the ResNet18/CIFAR-10 and PreActResNet18/TinyImageNet settings are presented in Figs. 4 and 5 in the Appendix. Figs. 1, 4 and 5 demonstrate that DAMP improves predictive accuracy over plain SGD across all corruptions without compromising accuracy on clean images. Although Fig. 1 indicates that

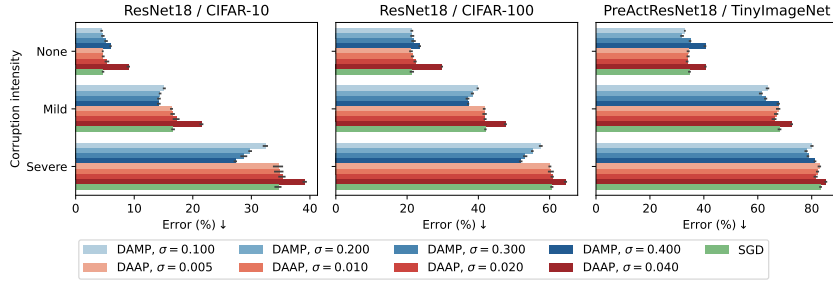


Figure 2: **DAMP has better corruption robustness than DAAP.** We report the predictive errors (lower is better) averaged over 5 seeds. None indicates no corruption. Mild includes severity levels 1, 2 and 3. Severe includes severity levels 4 and 5. We evaluate DAMP and DAAP under different noise standard deviations σ . These results imply that the multiplicative weight perturbations of DAMP are more effective than the additive perturbations of DAAP in improving robustness to corruptions.

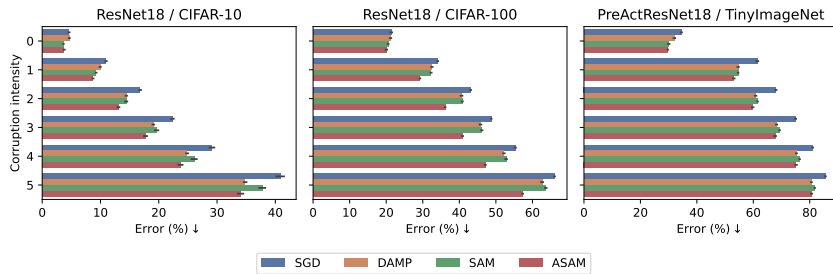


Figure 3: **DAMP surpasses SAM on corrupted images in most cases, despite requiring only half the training cost.** We report the predictive errors (lower is better) averaged over 5 seeds. A severity level of 0 indicates no corruption. We use the same number of epochs for all methods.

including `zoom_blur` as an augmentation when training ResNet18 on CIFAR-100 yields better results than DAMP on average, it also reduces accuracy on clean images and the brightness corruption. Overall, these figures show that incorporating a specific corruption as data augmentation during training enhances robustness to that particular corruption but may reduce performance on clean images and other corruptions. In contrast, DAMP consistently improves robustness across all corruptions. Notably, DAMP even enhances accuracy on clean images in the PreActResNet18/TinyImageNet setting, as shown in Fig. 5.

4.2 Comparing DAMP to random additive perturbations

In this section, we investigate whether additive weight perturbations can also enhance corruption robustness. To this end, we compare DAMP with its variant, Data Augmentation via Additive Perturbations (DAAP). Unlike DAMP, DAAP perturbs weights during training with random additive Gaussian noises centered at 0, as detailed in Algorithm 3 in the Appendix. Fig. 2 presents the results of DAMP and DAAP under different experimental settings, alongside standard SGD. Overall, Fig. 2 shows that across different experimental settings, the corruption robustness of DAAP is only slightly better than SGD and is worse than DAMP. Therefore, we conclude that multiplicative weight perturbations are better than their additive counterparts at improving robustness to corruptions.

4.3 Benchmark results

In this section, we compare DAMP with SGD, SAM (Foret et al., 2021), and ASAM (Kwon et al., 2021). For SAM and ASAM, we optimize the neighborhood size ρ by using 10% of the training set as a validation set. Similarly, we adjust the noise standard deviation σ for DAMP following the same procedure. For hyperparameters and additional training details, please refer to Appendix D.

Table 1: **DAMP surpasses the baselines on corrupted images in most cases.** We report the predictive errors (lower is better) averaged over 3 seeds for the ResNet50 / ImageNet experiments. For each level of severity in ImageNet-C and ImageNet- \bar{C} , we report the average error over all corruption types. We use 90 epochs and the basic Inception-style preprocessing for all experiments.

Method	ImageNet	ImageNet-C					ImageNet- \bar{C}				
		1	2	3	4	5	1	2	3	4	5
SGD	23.6 \pm 0.2	40.2 \pm 0.1	51.0 \pm 0.2	61.1 \pm 0.3	73.5 \pm 0.2	82.9 \pm <0.1	45.7 \pm 0.1	54.7 \pm 0.1	61.8 \pm <0.1	70.3 \pm 0.1	75.7 \pm 0.1
DAMP	23.8 \pm <0.1	38.2 \pm <0.1	48.1 \pm <0.1	57.4 \pm 0.2	69.5\pm0.3	79.9\pm0.2	42.4\pm0.1	51.2\pm0.1	58.6\pm<0.1	67.8\pm0.1	73.4\pm0.1
SAM	23.1 \pm 0.1	38.7 \pm 0.3	49.1 \pm 0.3	59.1 \pm 0.3	71.6 \pm 0.1	81.7 \pm 0.1	44.5 \pm <0.1	53.5 \pm 0.1	60.8 \pm <0.1	69.4 \pm <0.1	75.1 \pm 0.1
ASAM	22.8\pm0.1	37.4\pm0.1	47.5\pm<0.1	57.3\pm0.1	70.0 \pm 0.1	80.7 \pm 0.1	42.5 \pm 0.1	51.4 \pm 0.1	59.0 \pm 0.1	68.2 \pm 0.1	74.0 \pm <0.1

Table 2: **DAMP can train ViT-S16 on ImageNet from scratch, matching ResNet50’s accuracy in 200 epochs with only the basic Inception-style augmentations.** Due to the high training cost, we report the predictive error (lower is better) of a single run for the ViT-S16 / ImageNet experiments. For each level of corruption severity in ImageNet-C and ImageNet- \bar{C} , we report the average error over all corruption types. All experiments use only the basic Inception-style preprocessing.

Method	#Epochs	ImageNet	ImageNet-C					ImageNet- \bar{C}				
			1	2	3	4	5	1	2	3	4	5
AdamW	100	28.5	45.4	56.4	65.8	76.6	85.1	48.2	56.9	64.6	73.8	79.2
	200	28.7	46.4	58.0	67.1	77.4	85.6	48.6	57.2	64.9	74.0	79.4
DAMP	100	25.5	38.9	48.1	55.9	67.7	78.7	41.2	49.0	56.9	66.3	71.6
	200	23.7	36.7	45.7	53.3	65.4	76.8	39.6	47.6	55.6	64.9	70.3
SAM	100	23.9	35.9	45.0	53.2	65.9	77.8	39.8	47.9	55.8	65.3	70.8
ASAM	100	24.0	35.9	44.8	53.0	65.4	76.6	39.3	47.3	55.4	65.2	70.9

CIFAR-10/100 and TinyImageNet. Fig. 3 visualizes the predictive errors of DAMP and the baseline methods on CIFAR-10/100 and TinyImageNet, with all methods trained for the same number of epochs. It demonstrates that DAMP consistently outperforms SGD across various datasets and corruption severities, despite having the same training cost. Notably, DAMP outperforms SAM under most corruption scenarios, even though SAM takes twice as long to train and has higher accuracy on clean images. Additionally, DAMP improves accuracy on clean images over SGD on CIFAR-100 and TinyImageNet. Finally, ASAM consistently surpasses other methods on both clean and corrupted images, as it employs adversarial multiplicative weight perturbations (Section 3). However, like SAM, each ASAM experiment takes twice as long as DAMP given the same epoch counts.

ResNet50 / ImageNet Table 1 presents the predictive errors for the ResNet50 / ImageNet setting. It shows that DAMP consistently outperforms SAM under all corruption scenarios, despite having half the training cost and lower accuracy on clean images. Notably, DAMP surpasses the baselines on corrupted images in most cases, except for severity levels 1, 2, and 3 of ImageNet-C.

ViT-S16 / ImageNet Table 2 presents the predictive errors for the ViT-S16 / ImageNet setting, using the training setup from [Beyer et al. \(2022\)](#) but with only basic Inception-style preprocessing ([Szegedy et al., 2016](#)). Remarkably, DAMP can train ViT-S16 from scratch in 200 epochs to match ResNet50’s accuracy without advanced data augmentation. This is significant as ViT typically requires either extensive pretraining ([Dosovitskiy et al., 2021](#)), comprehensive data augmentation ([Beyer et al., 2022](#)), sophisticated training techniques ([Chen et al., 2022](#)), or modifications to the original architecture ([Yuan et al., 2021](#)) to perform well on ImageNet. Additionally, DAMP consistently ranks in the top 2 for corruption robustness across various test settings. Comparing Tables 1 and 2 reveals that ViT-S16 is more robust to corruptions than ResNet50 when both have similar performance on clean images.

5 Related works

Dropout Perhaps most relevant to our method is Dropout ([Srivastava et al., 2014](#)) and its many variants, such as DropConnect ([Wan et al., 2013](#)) and Variational Dropout ([Kingma et al., 2015](#)). These methods can be viewed as DAMP where the noise distribution Ξ is a structured multivariate Bernoulli distribution. For instance, Dropout multiplies all the weights connecting to a node with a binary random variable $p \sim \text{Bernoulli}(p)$. While the main motivation of these Dropout methods is to prevent co-adaptations of neurons to improve generalization on clean data, the motivation of DAMP

is to improve robustness to input corruptions without harming accuracy on clean data. Nonetheless, our experiments show that DAMP can improve generalization on clean data in certain scenarios, such as PreActResNet18/TinyImageNet and ViT-S16/ImageNet.

Ensemble methods Ensemble methods, such as Deep ensembles (Lakshminarayanan et al., 2017) and Bayesian neural networks (BNNs) (Graves, 2011; Blundell et al., 2015; Gal and Ghahramani, 2016; Louizos and Welling, 2017; Izmailov et al., 2021; Trinh et al., 2022), have been explored as effective defenses against corruptions. Ovadia et al. (2019) benchmarked some of these methods, demonstrating that they are more robust to corruptions compared to a single model. However, the training and inference costs of these methods increase linearly with the number of ensemble members, making them inefficient for use with very large DNNs.

Data augmentation Data augmentations aim at enhancing robustness include AugMix (Hendrycks et al., 2019), which combines common image transformations; Patch Gaussian (Lopes et al., 2019), which applies Gaussian noise to square patches; ANT (Rusak et al., 2020), which uses adversarially learned noise distributions for augmentation; and AutoAugment (Cubuk et al., 2018), which learns augmentation policies directly from the training data. These methods have been demonstrated to improve robustness to the corruptions in ImageNet-C (Hendrycks and Dietterich, 2019). Mintun et al. (2021) attribute the success of these methods to the fact that they generate augmented images perceptually similar to the corruptions in ImageNet-C and propose ImageNet-C, a test set of 10 new corruptions that are challenging to models trained by these augmentation methods.

Test-time adaptations via BatchNorm One effective approach to using unlabelled data to improve corruption robustness is to keep BatchNorm (Ioffe and Szegedy, 2015) on at test-time to adapt the batch statistics to the corrupted test data (Li et al., 2016; Nado et al., 2020; Schneider et al., 2020; Benz et al., 2021). A major drawback is that this approach cannot be used with BatchNorm-free architectures, such as Vision Transformer (Dosovitskiy et al., 2021).

6 Conclusion

In this work, we demonstrate that multiplicative weight perturbations improve robustness of DNNs to a wide range of input corruptions. We introduce DAMP, a simple training algorithm that perturbs weights during training with random multiplicative noises while maintaining the same training cost as standard SGD. We further show that ASAM (Kwon et al., 2021) can be viewed as optimizing DNNs under adversarial multiplicative weight perturbations. Our experiments show that both DAMP and ASAM indeed produce models that are robust to corruptions. DAMP is also shown to improve sample efficiency of Vision Transformer, allowing it to achieve comparable performance to ResNet50 on medium size datasets such as ImageNet without extensive data augmentations. As DAMP is domain-agnostic, one future direction is to explore its effectiveness in domains other than computer vision, such as natural language processing and reinforcement learning. Another direction is to explore alternative noise distributions to the Gaussian distribution used in our work.

Limitations Here we outline some limitations of this work. First, the proof of Theorem 1 assumes a simple feedforward neural network, thus it does not take into accounts modern DNN’s components such as normalization layers and attentions. Second, we did not evaluate DAMP in conjunction with advanced augmentation such as AugMix (Hendrycks et al., 2019) and AutoAugment (Cubuk et al., 2018). Finally, we only explored random Gaussian multiplicative perturbations, and there are likely more sophisticated noise distributions that could further boost corruption robustness.

Broader Impacts

Our paper introduces a new training method for neural networks that improves their robustness to input corruptions. Therefore, we believe that our work contributes towards making deep learning models safer and more reliable to use in real-world applications, especially those that are safety-critical. However, as with other methods that improve robustness, our method could also be improperly used in applications that negatively impact society, such as making mass surveillance systems more accurate and harder to fool. To this end, we hope that practitioners carefully consider issues regarding fairness, bias and other potentially harmful societal impacts when designing deep learning applications.

References

- Dan Hendrycks and Thomas Dietterich. Benchmarking neural network robustness to common corruptions and perturbations. *arXiv preprint arXiv:1903.12261*, 2019.
- Dario Amodei, Chris Olah, Jacob Steinhardt, Paul Christiano, John Schulman, and Dan Mané. Concrete problems in ai safety. *arXiv preprint arXiv:1606.06565*, 2016.
- Robert Geirhos, Carlos RM Temme, Jonas Rauber, Heiko H Schütt, Matthias Bethge, and Felix A Wichmann. Generalisation in humans and deep neural networks. *Advances in neural information processing systems*, 31, 2018.
- Ekin D Cubuk, Barret Zoph, Dandelion Mane, Vijay Vasudevan, and Quoc V Le. Autoaugment: Learning augmentation policies from data. *arXiv preprint arXiv:1805.09501*, 2018.
- Dan Hendrycks, Norman Mu, Ekin D Cubuk, Barret Zoph, Justin Gilmer, and Balaji Lakshminarayanan. Augmix: A simple data processing method to improve robustness and uncertainty. *arXiv preprint arXiv:1912.02781*, 2019.
- Raphael Gontijo Lopes, Dong Yin, Ben Poole, Justin Gilmer, and Ekin D Cubuk. Improving robustness without sacrificing accuracy with patch gaussian augmentation. *arXiv preprint arXiv:1906.02611*, 2019.
- Eric Mintun, Alexander Kirillov, and Saining Xie. On interaction between augmentations and corruptions in natural corruption robustness. In A. Beygelzimer, Y. Dauphin, P. Liang, and J. Wortman Vaughan, editors, *Advances in Neural Information Processing Systems*, 2021. URL <https://openreview.net/forum?id=L0Hyqjfyra>.
- Balaji Lakshminarayanan, Alexander Pritzel, and Charles Blundell. Simple and scalable predictive uncertainty estimation using deep ensembles. *Advances in neural information processing systems*, 30, 2017.
- Yaniv Ovadia, Emily Fertig, Jie Ren, Zachary Nado, D. Sculley, Sebastian Nowozin, Joshua Dillon, Balaji Lakshminarayanan, and Jasper Snoek. Can you trust your model's uncertainty? Evaluating predictive uncertainty under dataset shift. In H. Wallach, H. Larochelle, A. Beygelzimer, F. d'Alché-Buc, E. Fox, and R. Garnett, editors, *Advances in Neural Information Processing Systems*, volume 32. Curran Associates, Inc., 2019. URL https://proceedings.neurips.cc/paper_files/paper/2019/file/8558cb408c1d76621371888657d2eb1d-Paper.pdf.
- Michael Dusenberry, Ghassen Jerfel, Yeming Wen, Yian Ma, Jasper Snoek, Katherine Heller, Balaji Lakshminarayanan, and Dustin Tran. Efficient and scalable Bayesian neural nets with rank-1 factors. In Hal Daumé III and Aarti Singh, editors, *Proceedings of the 37th International Conference on Machine Learning*, volume 119 of *Proceedings of Machine Learning Research*, pages 2782–2792. PMLR, 13–18 Jul 2020. URL <https://proceedings.mlr.press/v119/dusenberry20a.html>.
- Trung Trinh, Markus Heinonen, Luigi Acerbi, and Samuel Kaski. Tackling covariate shift with node-based Bayesian neural networks. In Kamalika Chaudhuri, Stefanie Jegelka, Le Song, Csaba Szepesvari, Gang Niu, and Sivan Sabato, editors, *Proceedings of the 39th International Conference on Machine Learning*, volume 162 of *Proceedings of Machine Learning Research*, pages 21751–21775. PMLR, 17–23 Jul 2022.
- Jungmin Kwon, Jeongseop Kim, Hyunseo Park, and In Kwon Choi. Asam: Adaptive sharpness-aware minimization for scale-invariant learning of deep neural networks. In *International Conference on Machine Learning*, pages 5905–5914. PMLR, 2021.
- Alexey Dosovitskiy, Lucas Beyer, Alexander Kolesnikov, Dirk Weissenborn, Xiaohua Zhai, Thomas Unterthiner, Mostafa Dehghani, Matthias Minderer, Georg Heigold, Sylvain Gelly, Jakob Uszkoreit, and Neil Houlsby. An image is worth 16x16 words: Transformers for image recognition at scale. In *International Conference on Learning Representations*, 2021. URL <https://openreview.net/forum?id=YicbFdNTTy>.
- Kaiming He, Xiangyu Zhang, Shaoqing Ren, and Jian Sun. Deep residual learning for image recognition. In *IEEE conference on Computer Vision and Pattern Recognition*, 2016a.

- Christian Szegedy, Vincent Vanhoucke, Sergey Ioffe, Jon Shlens, and Zbigniew Wojna. Rethinking the inception architecture for computer vision. In *Proceedings of the IEEE conference on computer vision and pattern recognition*, pages 2818–2826, 2016.
- Xiangning Chen, Cho-Jui Hsieh, and Boqing Gong. When vision transformers outperform resnets without pre-training or strong data augmentations. In *International Conference on Learning Representations*, 2022. URL <https://openreview.net/forum?id=LtKcMgG0eLt>.
- Lucas Beyer, Xiaohua Zhai, and Alexander Kolesnikov. Better plain vit baselines for imagenet-1k. *arXiv preprint arXiv:2205.01580*, 2022.
- Pierre Foret, Ariel Kleiner, Hossein Mobahi, and Behnam Neyshabur. Sharpness-aware minimization for efficiently improving generalization. In *International Conference on Learning Representations*, 2021. URL <https://openreview.net/forum?id=6Tm1mposlrM>.
- Nitish Shirish Keskar, Dheevatsa Mudigere, Jorge Nocedal, Mikhail Smelyanskiy, and Ping Tak Peter Tang. On large-batch training for deep learning: Generalization gap and sharp minima. In *International Conference on Learning Representations*, 2017. URL <https://openreview.net/forum?id=H1oyRlYgg>.
- Yiding Jiang, Behnam Neyshabur, Hossein Mobahi, Dilip Krishnan, and Samy Bengio. Fantastic generalization measures and where to find them. In *International Conference on Learning Representations*, 2020. URL <https://openreview.net/forum?id=SJgIPJBFvH>.
- Alex Krizhevsky. Learning multiple layers of features from tiny images. Technical report, 2009.
- Ya Le and Xuan S. Yang. Tiny ImageNet visual recognition challenge. 2015.
- Jia Deng, Wei Dong, Richard Socher, Li-Jia Li, Kai Li, and Li Fei-Fei. Imagenet: A large-scale hierarchical image database. In *IEEE Conference on Computer Vision and Pattern Recognition*, pages 248–255, 2009. doi: 10.1109/CVPR.2009.5206848.
- Kaiming He, Xiangyu Zhang, Shaoqing Ren, and Jian Sun. Identity mappings in deep residual networks. In *European Conference on Computer Vision*, 2016b.
- Claudio Michaelis, Benjamin Mitzkus, Robert Geirhos, Evgenia Rusak, Oliver Bringmann, Alexander S. Ecker, Matthias Bethge, and Wieland Brendel. Benchmarking robustness in object detection: Autonomous driving when winter is coming. *arXiv preprint arXiv:1907.07484*, 2019.
- Li Yuan, Yunpeng Chen, Tao Wang, Weihao Yu, Yujun Shi, Zi-Hang Jiang, Francis EH Tay, Jiashi Feng, and Shuicheng Yan. Tokens-to-token vit: Training vision transformers from scratch on imagenet. In *Proceedings of the IEEE/CVF international conference on computer vision*, pages 558–567, 2021.
- Nitish Srivastava, Geoffrey Hinton, Alex Krizhevsky, Ilya Sutskever, and Ruslan Salakhutdinov. Dropout: A simple way to prevent neural networks from overfitting. *Journal of Machine Learning Research*, 15(56):1929–1958, 2014. URL <http://jmlr.org/papers/v15/srivastava14a.html>.
- Li Wan, Matthew Zeiler, Sixin Zhang, Yann Le Cun, and Rob Fergus. Regularization of neural networks using dropconnect. In Sanjoy Dasgupta and David McAllester, editors, *Proceedings of the 30th International Conference on Machine Learning*, volume 28 of *Proceedings of Machine Learning Research*, pages 1058–1066, Atlanta, Georgia, USA, 17–19 Jun 2013. PMLR. URL <https://proceedings.mlr.press/v28/wan13.html>.
- Durk P Kingma, Tim Salimans, and Max Welling. Variational dropout and the local reparameterization trick. *Advances in neural information processing systems*, 28, 2015.
- Alex Graves. Practical variational inference for neural networks. In J. Shawe-Taylor, R. Zemel, P. Bartlett, F. Pereira, and K.Q. Weinberger, editors, *Advances in Neural Information Processing Systems*, volume 24. Curran Associates, Inc., 2011. URL https://proceedings.neurips.cc/paper_files/paper/2011/file/7eb3c8be3d411e8ebfab08eba5f49632-Paper.pdf.

- Charles Blundell, Julien Cornebise, Koray Kavukcuoglu, and Daan Wierstra. Weight uncertainty in neural network. In *International conference on machine learning*, pages 1613–1622. PMLR, 2015.
- Yarin Gal and Zoubin Ghahramani. Dropout as a bayesian approximation: Representing model uncertainty in deep learning. In Maria Florina Balcan and Kilian Q. Weinberger, editors, *Proceedings of The 33rd International Conference on Machine Learning*, volume 48 of *Proceedings of Machine Learning Research*, pages 1050–1059, New York, New York, USA, 20–22 Jun 2016. PMLR. URL <https://proceedings.mlr.press/v48/gal16.html>.
- Christos Louizos and Max Welling. Multiplicative normalizing flows for variational bayesian neural networks. In *International Conference on Machine Learning*, pages 2218–2227. PMLR, 2017.
- Pavel Izmailov, Patrick Nicholson, Sanae Lotfi, and Andrew G Wilson. Dangers of bayesian model averaging under covariate shift. *Advances in Neural Information Processing Systems*, 34:3309–3322, 2021.
- Evgenia Rusak, Lukas Schott, Roland S Zimmermann, Julian Bitterwolf, Oliver Bringmann, Matthias Bethge, and Wieland Brendel. A simple way to make neural networks robust against diverse image corruptions. *arXiv preprint arXiv:2001.06057*, 2020.
- Sergey Ioffe and Christian Szegedy. Batch normalization: accelerating deep network training by reducing internal covariate shift. In *Proceedings of the 32nd International Conference on International Conference on Machine Learning - Volume 37, ICML’15*, page 448–456. JMLR.org, 2015.
- Yanghao Li, Naiyan Wang, Jianping Shi, Jiaying Liu, and Xiaodi Hou. Revisiting batch normalization for practical domain adaptation. *arXiv preprint arXiv:1603.04779*, 2016.
- Zachary Nado, Shreyas Padhy, D Sculley, Alexander D’Amour, Balaji Lakshminarayanan, and Jasper Snoek. Evaluating prediction-time batch normalization for robustness under covariate shift. *arXiv preprint arXiv:2006.10963*, 2020.
- Steffen Schneider, Evgenia Rusak, Luisa Eck, Oliver Bringmann, Wieland Brendel, and Matthias Bethge. Improving robustness against common corruptions by covariate shift adaptation. *Advances in neural information processing systems*, 33:11539–11551, 2020.
- Philipp Benz, Chaoning Zhang, Adil Karjauv, and In So Kweon. Revisiting batch normalization for improving corruption robustness. In *Proceedings of the IEEE/CVF winter conference on applications of computer vision*, pages 494–503, 2021.
- Dankmar Böhning and Bruce G Lindsay. Monotonicity of quadratic-approximation algorithms. *Annals of the Institute of Statistical Mathematics*, 40(4):641–663, 1988.

A Proof of Lemma 1

Here we provide the proof for Lemma 1 given the conditions and assumptions stated in Section 2:

Lemma. For all $h = 1, \dots, H$ and for all $\mathbf{x} \in \mathcal{X}$, there exists a scalar $C_{\mathbf{g}}^{(h)}(\mathbf{x}) > 0$ such that:

$$\delta_{\mathbf{g}}\ell(\boldsymbol{\omega}, \mathbf{x}, y) \leq \left\langle \nabla_{\mathbf{z}^{(h+1)}}\ell(\boldsymbol{\omega}, \mathbf{x}, y) \otimes \delta_{\mathbf{g}}\mathbf{f}^{(h)}(\mathbf{x}), \mathbf{W}^{(h+1)} \right\rangle_F + \frac{C_{\mathbf{g}}^{(h)}(\mathbf{x})}{2} \|\mathbf{W}^{(h)}\|_F^2 \quad (28)$$

Proof. Here we note that:

$$\delta_{\mathbf{g}}\ell(\boldsymbol{\omega}, \mathbf{x}, y) \stackrel{\text{def}}{=} \ell(\boldsymbol{\omega}, \mathbf{g}(\mathbf{x}), y) - \ell(\boldsymbol{\omega}, \mathbf{x}, y) \quad (29)$$

$$\delta_{\mathbf{g}}\mathbf{f}^{(h)}(\mathbf{x}) \stackrel{\text{def}}{=} \mathbf{f}^{(h)}(\mathbf{g}(\mathbf{x})) - \mathbf{f}^{(h)}(\mathbf{x}) \quad (30)$$

We first notice that the per-sample loss $\ell(\boldsymbol{\omega}, \mathbf{x}, y)$ can be viewed as a function of the intermediate activation $\mathbf{f}^{(h)}(\mathbf{x})$ of layer h . From Assumption 2, there exists a constant $L_h > 0$ such that:

$$\|\nabla_{\mathbf{f}^{(h)}}\ell(\boldsymbol{\omega}, \mathbf{g}(\mathbf{x}), y) - \nabla_{\mathbf{f}^{(h)}}\ell(\boldsymbol{\omega}, \mathbf{x}, y)\|_2 \leq L_h \|\mathbf{f}^{(h)}(\mathbf{g}(\mathbf{x})) - \mathbf{f}^{(h)}(\mathbf{x})\|_2 \quad (31)$$

which gives us the following quadratic bound:

$$\ell(\boldsymbol{\omega}, \mathbf{g}(\mathbf{x}), y) \leq \ell(\boldsymbol{\omega}, \mathbf{x}, y) + \left\langle \nabla_{\mathbf{f}^{(h)}}\ell(\boldsymbol{\omega}, \mathbf{x}, y), \delta_{\mathbf{g}}\mathbf{f}^{(h)}(\mathbf{x}) \right\rangle + \frac{L_h}{2} \|\delta_{\mathbf{g}}\mathbf{f}^{(h)}(\mathbf{x})\|_2^2 \quad (32)$$

where $\langle \cdot, \cdot \rangle$ denotes the dot product between two vectors. The results in the equation above have been proven in Böhning and Lindsay (1988). We thus have:

$$\delta_{\mathbf{g}}\ell(\boldsymbol{\omega}, \mathbf{x}, y) \leq \left\langle \nabla_{\mathbf{f}^{(h)}}\ell(\boldsymbol{\omega}, \mathbf{x}, y), \delta_{\mathbf{g}}\mathbf{f}^{(h)}(\mathbf{x}) \right\rangle + \frac{L_h}{2} \|\delta_{\mathbf{g}}\mathbf{f}^{(h)}(\mathbf{x})\|_2^2 \quad (33)$$

Since the pre-activation output of layer $h + 1$ is $\mathbf{z}^{(h+1)}(\mathbf{x}) = \mathbf{W}^{(h+1)}\mathbf{f}^{(h)}(\mathbf{x})$, we can rewrite the inequality above as:

$$\delta_{\mathbf{g}}\ell(\boldsymbol{\omega}, \mathbf{x}, y) \leq \left\langle \nabla_{\mathbf{z}^{(h+1)}}\ell(\boldsymbol{\omega}, \mathbf{x}, y) \otimes \delta_{\mathbf{g}}\mathbf{f}^{(h)}(\mathbf{x}), \mathbf{W}^{(h+1)} \right\rangle_F + \frac{L_h}{2} \|\delta_{\mathbf{g}}\mathbf{f}^{(h)}(\mathbf{x})\|_2^2 \quad (34)$$

where \otimes denotes the outer product of two vectors and $\langle \cdot, \cdot \rangle_F$ denotes the Frobenius inner product of two matrices of similar dimension.

From Assumption 1, we have that there exists a constant $M > 0$ such that:

$$\|\delta_{\mathbf{g}}\mathbf{f}^{(0)}(\mathbf{x})\|_2^2 = \|\mathbf{g}(\mathbf{x}) - \mathbf{x}\|_2^2 \leq M \quad (35)$$

Given that $\mathbf{f}^{(1)}(\mathbf{x}) = \boldsymbol{\sigma}^{(1)}(\mathbf{W}^{(1)}\mathbf{f}^{(0)}(\mathbf{x}))$, we have:

$$\|\delta_{\mathbf{g}}\mathbf{f}^{(1)}(\mathbf{x})\|_2^2 = \|\mathbf{f}^{(1)}(\mathbf{g}(\mathbf{x})) - \mathbf{f}^{(1)}(\mathbf{x})\|_2^2 \leq \|\mathbf{W}^{(1)}\delta_{\mathbf{g}}\mathbf{f}^{(0)}(\mathbf{x})\|_2^2 \quad (36)$$

Here we assume that the activate $\boldsymbol{\sigma}$ satisfies $\|\boldsymbol{\sigma}(\mathbf{x}) - \boldsymbol{\sigma}(\mathbf{y})\|_2 \leq \|\mathbf{x} - \mathbf{y}\|_2$, which is true for modern activation functions such as ReLU. Since $\|\delta_{\mathbf{g}}\mathbf{f}^{(0)}(\mathbf{x})\|_2^2$ is bounded, there exists a constant $\hat{C}_{\mathbf{g}}^{(1)}(\mathbf{x})$ such that:

$$\|\delta_{\mathbf{g}}\mathbf{f}^{(1)}(\mathbf{x})\|_2^2 = \|\mathbf{f}^{(1)}(\mathbf{g}(\mathbf{x})) - \mathbf{f}^{(1)}(\mathbf{x})\|_2^2 \leq \|\mathbf{W}^{(1)}\delta_{\mathbf{g}}\mathbf{f}^{(0)}(\mathbf{x})\|_2^2 \leq \frac{\hat{C}_{\mathbf{g}}^{(1)}(\mathbf{x})}{2} \|\mathbf{W}^{(1)}\|_F^2 \quad (37)$$

where $\|\cdot\|_F$ denotes the Frobenius norm. Similarly, as we have proven that $\|\delta_{\mathbf{g}}\mathbf{f}^{(1)}(\mathbf{x})\|_2^2$ is bounded, there exists a constant $\hat{C}_{\mathbf{g}}^{(2)}(\mathbf{x})$ such that:

$$\|\delta_{\mathbf{g}}\mathbf{f}^{(2)}(\mathbf{x})\|_2^2 = \|\mathbf{f}^{(2)}(\mathbf{g}(\mathbf{x})) - \mathbf{f}^{(2)}(\mathbf{x})\|_2^2 \leq \|\mathbf{W}^{(2)}\delta_{\mathbf{g}}\mathbf{f}^{(1)}(\mathbf{x})\|_2^2 \leq \frac{\hat{C}_{\mathbf{g}}^{(2)}(\mathbf{x})}{2} \|\mathbf{W}^{(2)}\|_F^2 \quad (38)$$

Thus we have proven that for all $h = 1, \dots, H$, there exists a constant $\hat{C}_{\mathbf{g}}^{(h)}(\mathbf{x})$ such that:

$$\|\delta_{\mathbf{g}}\mathbf{f}^{(h)}(\mathbf{x})\|_2^2 \leq \frac{\hat{C}_{\mathbf{g}}^{(h)}(\mathbf{x})}{2} \|\mathbf{W}^{(h)}\|_F^2 \quad (39)$$

By combining Eqs. (34) and (39) and setting $C_{\mathbf{g}}^{(h)}(\mathbf{x}) = L_h \hat{C}_{\mathbf{g}}^{(h)}(\mathbf{x})$, we arrive at Eq. (28). \square

Algorithm 2 Training with corruption

- 1: **Input:** training data $\mathcal{S} = \{(\mathbf{x}_k, y_k)\}_{k=1}^N$, a neural network $f(\cdot; \omega)$ parameterized by $\omega \in \mathbb{R}^P$, number of iterations T , step sizes $\{\eta_t\}_{t=1}^T$, batch size B , a corruption \mathbf{g} such as Gaussian noise, weight decay coefficient λ , a loss function $\mathcal{L} : \mathbb{R}^P \rightarrow \mathbb{R}_+$.
 - 2: **Output:** Optimized parameter $\omega^{(T)}$.
 - 3: Initialize parameter $\omega^{(0)}$.
 - 4: **for** $t = 1$ **to** T **do**
 - 5: Draw a mini-batch $\mathcal{B} = \{\mathbf{x}_b, y_b\}_{b=1}^B \sim \mathcal{S}$.
 - 6: Divide the mini-batch into two disjoint sub-batches of equal size \mathcal{B}_1 and \mathcal{B}_2 .
 - 7: Apply the corruption \mathbf{g} to all samples in \mathcal{B}_1 : $\mathbf{g}(\mathcal{B}_1) = \{(\mathbf{g}(\mathbf{x}), y)\}_{(\mathbf{x}, y) \in \mathcal{B}_1}$.
 - 8: Compute the gradient $\mathbf{g} = \nabla_{\omega} \mathcal{L}(\omega; \mathbf{g}(\mathcal{B}_1) \cup \mathcal{B}_2)$.
 - 9: Update the weights: $\omega^{(t+1)} = \omega^{(t)} - \eta_t (\mathbf{g} + \lambda \omega^{(t)})$.
 - 10: **end for**
-

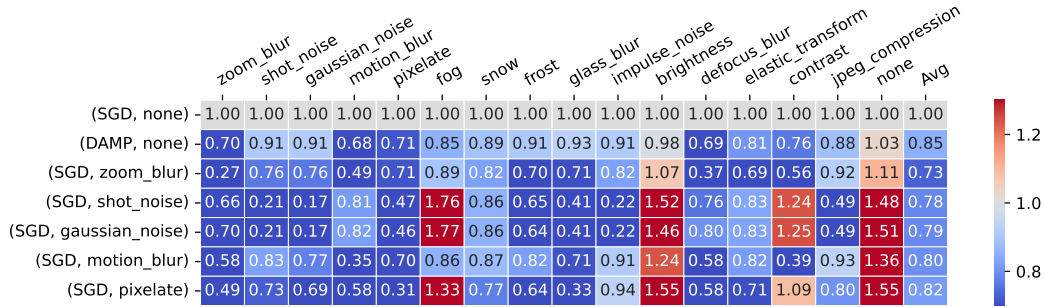


Figure 4: **DAMP improves robustness to all corruptions while preserving accuracy on clean images.** Results of ResNet18/CIFAR-10 experiments averaged over 3 seeds. The heatmap shows CE_c^f described in Eq. (27), where each row corresponds to a tuple of training (method, corruption), while each column corresponds to the test corruption. The Avg column shows the average of the results of the previous columns. none indicates no corruption. We use the models trained under the SGD/none setting (first row) as baselines to calculate the CE_c^f . The last five rows are the 5 best training corruptions ranked by the results in the Avg column.

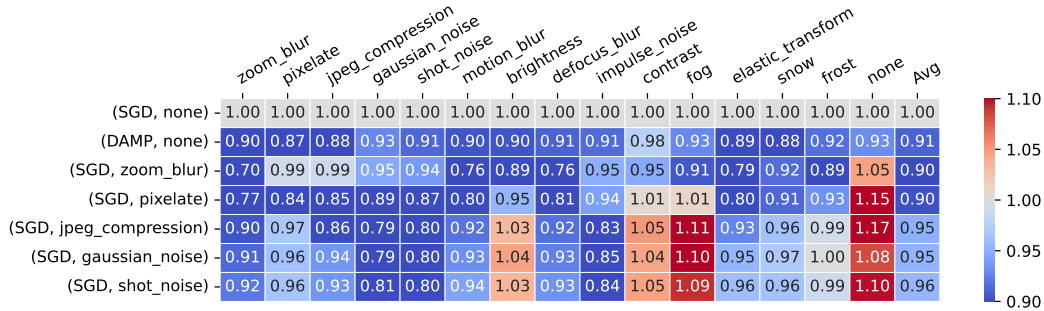


Figure 5: **DAMP improves robustness to all corruptions while preserving accuracy on clean images.** Results of PreActResNet18/TinyImageNet experiments averaged over 3 seeds. The heatmap shows CE_c^f described in Eq. (27), where each row corresponds to a tuple of training (method, corruption), while each column corresponds to the test corruption. The Avg column shows the average of the results of the previous columns. none indicates no corruption. We use the models trained under the SGD/none setting (first row) as baselines to calculate the CE_c^f . The last five rows are the 5 best training corruptions ranked by the results in the Avg column.

B Training with corruption

Here we present Algorithm 2 which uses corruptions as data augmentation during training, as well as the experiment results of Section 4.1 for ResNet18/CIFAR-10 and PreActResNet18/TinyImageNet settings in Figs. 4 and 5.

C Training with random additive weight perturbations

Here, we present Algorithm 3 used in Section 4.2 which trains DNNs under random additive weight perturbations.

Algorithm 3 DAAP: Data Augmentation via Additive Perturbations

- 1: **Input:** training data $\mathcal{S} = \{\mathbf{x}_k, y_k\}_{k=1}^N$, a neural network $\mathbf{f}(\cdot; \boldsymbol{\omega})$ parameterized by $\boldsymbol{\omega} \in \mathbb{R}^P$, number of iterations T , step sizes $\{\eta_t\}_{t=1}^T$, number of sub-batch M , batch size B divisible by M , a noise distribution $\Xi = \mathcal{N}(\mathbf{0}, \sigma^2 \mathbf{I}_P)$, weight decay coefficient λ , a loss function $\mathcal{L} : \mathbb{R}^P \rightarrow \mathbb{R}_+$.
 - 2: **Output:** Optimized parameter $\boldsymbol{\omega}^{(T)}$.
 - 3: Initialize parameter $\boldsymbol{\omega}^{(0)}$.
 - 4: **for** $t = 1$ **to** T **do**
 - 5: Draw a mini-batch $\mathcal{B} = \{\mathbf{x}_b, y_b\}_{b=1}^B \sim \mathcal{S}$.
 - 6: Divide the mini-batch into M disjoint sub-batches $\{\mathcal{B}_m\}_{m=1}^M$ of equal size.
 - 7: **for** $m = 1$ **to** M **in parallel do**
 - 8: Draw a noise sample $\boldsymbol{\xi}_m \sim \Xi$.
 - 9: Compute the gradient $\mathbf{g}_m = \nabla_{\boldsymbol{\omega}} \mathcal{L}(\boldsymbol{\omega}; \mathcal{B}_m)|_{\boldsymbol{\omega}^{(t)} + \boldsymbol{\xi}}$.
 - 10: **end for**
 - 11: Compute the average gradient: $\mathbf{g} = \frac{1}{M} \sum_{m=1}^M \mathbf{g}_m$.
 - 12: Update the weights: $\boldsymbol{\omega}^{(t+1)} = \boldsymbol{\omega}^{(t)} - \eta_t (\mathbf{g} + \lambda \boldsymbol{\omega}^{(t)})$.
 - 13: **end for**
-

D Training details

For each method and each setting, we tune the important hyperparameters (σ for DAMP, ρ for SAM and ASAM) using 10% of the training set as validation set.

CIFAR-10/100 For each setting, we train a ResNet18 for 300 epochs. We use a batch size of 128. We use a learning rate of 0.1 and a weight decay coefficient of 5×10^{-4} . We use SGD with Nesterov momentum as the optimizer with a momentum coefficient of 0.9. The learning rate is kept at 0.1 until epoch 150, then is linearly annealed to 0.001 from epoch 150 to epoch 270, then kept at 0.001 for the rest of the training. We use basic data preprocessing, which includes channel-wise normalization, random cropping after padding and random horizontal flipping. On CIFAR-10, we set $\sigma = 0.2$ for DAMP, $\rho = 0.045$ for SAM and $\rho = 1.0$ for ASAM. On CIFAR-100, we set $\sigma = 0.1$ for DAMP, $\rho = 0.06$ for SAM and $\rho = 2.0$ for ASAM. Each method is trained on a single host with 8 Nvidia V100 GPUs where the data batch is evenly distributed among the GPUs at each iteration (data parallelism). This means we use the number of sub-batches $M = 8$ for DAMP.

TinyImageNet For each setting, we train a PreActResNet18 for 150 epochs. We use a batch size of 128. We use a learning rate of 0.1 and a weight decay coefficient of 2.5×10^{-4} . We use SGD with Nesterov momentum as the optimizer with a momentum coefficient of 0.9. The learning rate is kept at 0.1 until epoch 75, then is linearly annealed to 0.001 from epoch 75 to epoch 135, then kept at 0.001 for the rest of the training. We use basic data preprocessing, which includes channel-wise normalization, random cropping after padding and random horizontal flipping. We set $\sigma = 0.2$ for DAMP, $\rho = 0.2$ for SAM and $\rho = 3.0$ for ASAM. Each method is trained on a single host with 8 Nvidia V100 GPUs where the data batch is evenly distributed among the GPUs at each iteration (data parallelism). This means we use the number of sub-batches $M = 8$ for DAMP.

ResNet50 / ImageNet We train each experiment for 90 epochs. We use a batch size of 2048. We use a weight decay coefficient of 1×10^{-4} . We use SGD with Nesterov momentum as the optimizer with a momentum coefficient of 0.9. We use basic Inception-style data preprocessing, which includes random cropping, resizing to the resolution of 224×224 , random horizontal flipping and channel-wise normalization. We increase the learning rate linearly from 8×10^{-4} to 0.8 for the first 5 epochs then decrease the learning rate from 0.8 to 8×10^{-4} using a cosine schedule for the remaining epochs. All experiments were run on a single host with 8 Nvidia V100 GPUs and we set $M = 8$ for DAMP. We use $\sigma = 0.1$ for DAMP, $\rho = 0.05$ for SAM, and $\rho = 1.5$ for ASAM. We also use the image resolution of 224×224 during evaluation.

ViT-S16 / ImageNet We follow the training setup of [Beyer et al. \(2022\)](#) with one difference is that we only use basic Inception-style data processing similar to the ResNet50/ImageNet experiments. We use AdamW as the optimizer with $\beta_1 = 0.9$, $\beta_2 = 0.999$ and $\epsilon = 10^{-8}$. We clip the gradient norm to 1.0. We use a weight decay coefficient of 0.1. We use a batch size of 1024. We increase the learning rate linearly from 10^{-6} to 10^{-3} for the first 10000 iterations, then we anneal the learning rate from 10^{-3} to 0 using a cosine schedule for the remaining iterations. We use the image resolution of 224×224 for both training and testing. Following [Beyer et al. \(2022\)](#), we make 2 minor modifications to the original ViT-S16 architecture: (1) We change the position embedding layer from `learnable` to `sincos2d`; (2) We change the input of the final classification layer from the embedding of the `[cls]` token to global average-pooling. All experiments were run on a single host with 8 Nvidia V100 GPUs and we set $M = 8$ for DAMP. We use $\sigma = 0.25$ for DAMP, $\rho = 0.6$ for SAM, and $\rho = 3.0$ for ASAM.